THE ASTROPHYSICAL JOURNAL, 361:596–606, 1990 October 1

EXOSAT OBSERVATIONS OF CYGNUS X-2 CONTINUUM AND LINE SPECTRUM

L. CHIAPPETTI,[1] A. TREVES,[2] G. BRANDUARDI-RAYMONT,[3] A. L. CIAPI,[2] E. N. ERCAN,[4] P. E. FREEMAN,[5] S. M. KAHN,[5] L. MARASCHI,[2] F. B. S. PAERELS,[5,6] AND E. G. TANZI[1]

Received 1989 November 27; accepted 1990 March 28

ABSTRACT

We present an analysis of five *EXOSAT* observations of Cyg X-2, taken around a full binary orbit. The data were obtained using all instrumentation (1000 lines mm^{-1} Transmission Grating Spectrometer, Channel Multiplier Array + filters, Medium-Energy experiment, Gas Scintillation Proportional Counter) simultaneously, and span the full energy range 0.5–20 keV. We find no clear evidence for a correlation of any of the source characteristics with orbital phase. During two of our observations significant iron K emission at 6.7 keV was detected, the relative strength of which seems to correlate with total X-ray intensity during two sharp intensity dips. We confirm the previous detection of discrete emission features in the 12–19 Å band with the *Einstein* grating.

Subject headings: stars: individual (Cyg X-2) — X-rays: binaries

I. INTRODUCTION

Extensive observations of Cyg X-2 since its discovery nearly 25 years ago have established that it is a low-mass X-ray binary (LMXB). It consists of a neutron star of mass $\sim 1.4\ M_\odot$, accompanied by a late-type, evolved low-mass ($\sim 0.7\ M_\odot$) star in a 9.84 day binary orbit (Bradt and McClintock 1983; Cowley, Crampton, and Hutchings 1979, hereafter CCH). The evolution of the binary is believed to be driven by the secular expansion of the giant secondary, which transfers mass via a disk onto the neutron star through overflow of its Roche-lobe (Webbink, Rappaport, and Savonije 1983).

The temporal behavior of the X-ray emission from Cyg X-2 is complicated. It shows both high- and low-intensity states and irregular intensity dips. No persistent modulation of the X-ray flux at the binary period has been found. In addition, Cyg X-2 shows rapid, quasi-periodic oscillations (QPOs) in hard (2–20 keV) X-rays (Hasinger *et al.* 1986).

Analysis of the X-ray spectral properties in terms of X-ray intensity hardness, and X-ray color-color plots, has revealed complex behavior. Part of the time the source is found to move along a well-defined, Z-shaped track in X-ray color-color diagrams, on a time scale of days. QPO characteristics correlate with the position of the source on the Z (see van der Klis 1989 for a recent review of LMXB spectral and QPO behavior). However, at the other epochs the source has been found in positions on the color-color diagram that are apparently not related to the Z (see the data presented by Vrtilek *et al.* 1986).

Like the other LMXBs, Cyg X-2 shows a complex X-ray spectrum. Characterization of its 2–20 keV spectrum generally requires a superposition of several spectral components. Composite models, comprising either a thermal bremsstrahlung continuum together with a blackbody, two blackbodies, power law plus thermal bremsstrahlung, a multitemperature blackbody disk spectrum plus boundary layer blackbody, or a Comptonized spectrum, have all been found to describe the data roughly equally well (Vrtilek *et al.* 1986; Mitsuda *et al.* 1984; White, Stella, and Parmar 1988). It is unclear at present which of these models, if any at all, represent the underlying X-ray emission mechanism, and whether the spectral components can be uniquely assigned to the various physical emission regions in the system (e.g., disk, magnetospheric boundary layer, disk corona, neutron star surface; White, Stella, and Parmar 1988).

Observations with the *Einstein* Objective Grating Spectrometer (OGS; Vrtilek *et al.* 1986) have revealed discrete emission and absorption features in the 0.5–2 keV band. However, due to the rather limited resolution and statistical quality of the OGS data, no definite line identifications could be made, and consequently the origin of the line emission (arising in either a photoionized or a collisionally ionized plasma) has not yet been determined with any certainty.

The instrumentation carried on *EXOSAT* provided a unique combination of wide-energy range coverage with moderate spectral resolution. We describe an extensive set of X-ray spectral data on Cyg X-2, obtained with *EXOSAT* over a complete binary orbit, using all the available instruments on the observatory (the Low-Energy telescopes [LE], both with and without the 1000 lines mm^{-1} Transmission Grating Spectrometer [TGS] in the beam, the Medium-Energy proportional counter array [ME], and the Gas Scintillation Proportional Counter [GSPC]). The data cover the full 0.5–20 keV band simultaneously.

The remainder of this paper is organized as follows. In § II we give a brief description of the *EXOSAT* instruments, and an overview of the observations. Section III contains a discussion of the data reduction procedures and a presentation of light curves. In § IV we discuss the continuum spectrum, and the detection of discrete emission lines, both with the GSPC and the TGS. In § V we report on far UV observations simultaneous with the X-ray ones. In § VI we briefly discuss our results.

[1] Istituto di Fisica Cosmica, CNR, Milan, Italy.
[2] Dipartimento di Fisica dell'Universitá, Milan, Italy.
[3] Mullard Space Science Laboratory, University College London, Holmbury St. Mary, Great Britain.
[4] Boğaziçi University, Bebek, Istanbul, Turkey.
[5] Department of Physics and Space Sciences Laboratory, University of California, Berkeley, California.
[6] Institute of Geophysics and Planetary Physics, Lawrence Livermore National Laboratory, California.

Some of the results presented here were shortly reported at meetings (Chiappetti *et al.* 1987; Freeman *et al.* 1989), while the analysis of QPOs in our data is discussed in Stella *et al.* (1986).

II. INSTRUMENTATION AND OBSERVATIONS

EXOSAT carried two identical soft X-ray imaging telescopes, LE1 and LE2, sensitive in the range 0.04–2 keV. They consisted of double-nested Wolter-I grazing incidence mirror assemblies, of focal length 109 cm, and 90.5 cm^2 total geometric area. The focal plane images were registered with a Channel Multiplier Array (CMA), and a filter wheel placed directly in front of the CMAs offered the choice between 5 different broad-band photometric filters. The telescopes with the "general purpose" thin Lexan filter had maximum effective area ~ 10 cm^2 around 0.16 keV (80 Å); in the band shortward of 0.5 keV (23 Å) the area peaked at ~ 4 cm^2.

Both telescopes were equipped with a free-standing gold transmission grating, of 1000 lines mm^{-1} (LE1), and 500 lines mm^{-1} (LE2), respectively, that could be rotated into the focused X-ray beam exiting the mirror assemblies, thus converting them to TGSs. The gratings had efficiency for diffraction into first order of ~ 0.1; they were blazed to enhance the efficiency in the 1–2 keV band. The resolution in the 0.5–2 keV (5–23 Å) band was constant in wavelength, being dominated by the optics imaging properties, at $\Delta\lambda \sim 1.25$ Å (2.5 Å) for the 1000 lines mm^{-1} (500 lines mm^{-1}) grating. A general description of the LE instruments and their calibration can be found in de Korte *et al.* (1981) and Paerels *et al.* (1989).

The ME (Turner, Smith, and Zimmerman 1981) consisted of eight separate multiwire detectors, each comprising an argon and a xenon chamber. The argon chambers were sensitive in the band 1–20 keV, the xenon chambers in the band 5–50 keV. The ME had a total geometric area of ~ 1600 cm^2. Anticoincidence and risetime discrimination techniques ensured very good particle background rejection efficiency; the residual background could be monitored by slightly offsetting half of the detector array. The argon counters had an energy resolution of $\Delta E/E = 0.21$ at 6 keV, the Xenon counters had $\Delta E/E = 0.18$ at 22 keV.

The GSPC (Peacock *et al.* 1981) covered approximately the same energy range as the ME (either 2–16 or 2–32 keV, according to the gain setting), but had a factor of 2 higher resolution ($\Delta E/E = 0.11$ at 6 keV). Its effective area was much lower, however, reaching 100 cm^2 at maximum.

Further details concerning the mission and the instruments can be found in White and Peacock (1988).

Table 1 gives a journal of the observations discussed in this paper. In all, we had five observations of ~ 2 hr each (hereafter referred to by their sequence number in Table 1), roughly equally spaced around the 9.8 day binary orbit. Details con-

TABLE 1

OBSERVATIONS OF CYG X-2 WITH *EXOSAT*

A. LOW ENERGY

Observation Number	Start Time (UT) Date (1983)	Start Time (UT) Times	End Time (UT)	Exposure Time (s)	Count Rate (counts s^{-1})	Filter	Notes
			LE1 (CMA)				
1	Sep 13	23:17	01:04	6355	...	3Lexan	grating
2	Sep 15	19:29	20:10	6451	...	3Lexan	grating jammed
3	Sep 18	...	...	...	...	...	not operative
4	Sep 20	23:30	01:17	6128	3.16 ± 0.03	3Lexan	
5	Sep 22	16:39	19:04	7367	3.07 ± 0.02	3Lexan	
			LE2 (CMA)				
1	Sep 13	23:20	23:41	690	6.25 ± 0.10	3Lexan	
		23:45	00:08	990	4.25 ± 0.07	Al/Par	
	Sep 14	00:12	00:34	1008	3.45 ± 0.06	Boron	
		00:39	01:05	1089	6.05 ± 0.08	PPL	
2	Sep 15	19:26	20:05	929	6.20 ± 0.09	3Lexan	
		20:08	20:38	1232	4.48 ± 0.07	Al/Par	
		20:41	20:56	1275	3.31 ± 0.10	Boron	no dip
		20:57	21:09		1.84 ± 0.10	Boron	dip
		21:13	21:26	1893	3.63 ± 0.10	PPL	dip
		21:33	22:03		5.05 ± 0.10	PPL	no dip
3	Sep 18	16:31	16:57	931	3.80 ± 0.07	3Lexan	
		17:00	17:25	1043	2.84 ± 0.06	Al/Par	
		17:28	17:54	1206	2.06 ± 0.05	Boron	
		17:56	19:09	2809	3.72 ± 0.04	PPL	
4	Sep 20	23:24	23:57	1233	4.62 ± 0.07	3Lexan	
	Sep 21	00:00	00:23	923	3.32 ± 0.07	Al/Par	
		00:26	00:48	974	2.42 ± 0.06	Boron	
		00:55	01:19	928	4.33 ± 0.07	PPL	
5	Sep 22	16:35	16:58	1358	4.26 ± 0.06	3Lexan	
		17:02	17:24	1319	3.16 ± 0.05	Al/Par	
		17:28	17:55	1577	2.33 ± 0.04	Boron	
		17:59	19:05	3522	4.09 ± 0.04	PPL	

TABLE 1—*Continued*

B. ME (ARGON AND XENON)

Observation Number	Start Time Date (1983)	Start Time Time	End Time (UT)	Exposure Time (s) Ar	Exposure Time (s) Xe	Count Rate (counts s^{-1} $half^{-1}$) Ar	Count Rate (counts s^{-1} $half^{-1}$) Xe	Half Experiment	Notes
1.....	Sep 13	23:03	23:59	3313	3313	962 ± 0.6	30.6 ± 0.3	H2	
	Sep 14	00:07	01:08	3648	3648	1009 ± 0.6	30.3 ± 0.3	H1	
2.....	Sep 15	18:47	19:52	2957	2952	979 ± 0.7	29.6 ± 0.3	H2	
		19:52	20:30	...	...	...	...	H2	ADC problem
		20:37	22:09	...	...	...	...	H1	ADC problem
3.....	Sep 18	16:05	19:13	9831	...	610 ± 0.3	...	H2	
		17:09	19:13	...	6413	...	39.2 ± 0.3	H2	
4.....	Sep 20	23:22	01:36	7316	...	967 ± 0.4	...	H1	
		23:22	00:38	...	4568	...	55.0 ± 0.3	H1	
5.....	Sep 22	15:51	19:09	9816	...	899 ± 0.4	...	H2	
		15:51	17:28	...	4863	...	54.5 ± 0.2	H2	

C. GSPC

Observation Number	Start Time Date (1983)	Start Time Time	End Time (UT)	Exposure Time (s)	Count Rate (counts s^{-1})	Notes
1.....	Sep 13	23:06	01:07	7208	79.9 ± 0.1	no dip
	Sep 14	01:14	01:28	736	71.0 ± 0.4	dip
2.....	Sep 15	18:48	21:04	7656	82.5 ± 0.1	no dip
		21:06	21:26	1200	64.3 ± 0.3	dip
3.....	Sep 18	16:04	19:17	9432	64.9 ± 0.1	
4.....	Sep 20	23:16	01:36	7672	84.9 ± 0.1	
5.....	Sep 22	13:45	20:32	9272	86.3 ± 0.1	

NOTES.—For the low-energy experiments the count rate is given for all observations except the grating ones. The filters abbreviations refer respectively, to 3000 Å Lexan, aluminum-parylene, boron, and polypropilene filters. For the medium-energy experiment the count rate is given in each half experiment, as applicable, respectively in the ranges 1–17 keV (PHA channels 5–58) for argon and 7–20 keV (PHA channels 18–48) for xenon.

cerning instrumental configurations are given in Table 1. Assuming the ephemeris by Crampton and Cowley (1980), J.D. = 2,443,162.1, $P = 9.844$ day, the five observations are, respectively, centered at phase 0.8, 0.0, 0.3, 0.5, and 0.7.

The broadest spectral coverage (LE grating spectrum in addition to ME and GSPC spectral data) was available during observation 1 only. Because of a failure of the grating mechanism in LE1 immediately after our first observation, the gratings were not moved afterward, and only broad-band filter data were available at the lowest energies. Part of the ME data obtained during observation 2 were corrupted due to an operational error, an electronics switch being improperly used (referred hereafter as ADC problem). They were not used for the present analysis.

The ME was operated for most of the time in a mode collecting one full-resolution 128 pulse height channels Ar and Xe spectrum per half experiment every 2.5 s. For about one third of observations 3, 4, and 5 we used a compressed submode (where a 32 bin argon-only spectrum, covering the channel range 5–68, per half experiment, was collected every 0.3125 s). This explains the different exposure times for argon and xenon spectra. In order to combine all argon data together, all spectra were compressed on the ground to 32 bins in the same range used by the compressed mode on-board.

III. DATA REDUCTION PROCEDURES; LE, ME, AND GSPC LIGHT CURVES

Overall LE count rates (as reported in Table 1) were derived as follows: first a preliminary background was derived in concentric boxes of sides 50 and 75 pixels around the approximate source position, then the source centroid was located. A program was run to derive at the same time the point spread function and the background. The final count rates were extracted from a box of 25 pixels size. They were corrected for point spread function, dead time, vignetting, and background nonuniformity effects. The LE light curves were derived in a box of 25 pixels side, while the background was measured in a surrounding box of 50 pixels outer side. Dead-time instantaneous corrections were applied during the light curve accumulation. Corrections for all other effects were applied post facto. There is no evidence for large variability in the light curves of the individual observations, except for a broad dip in observation 2 (which is presented in Fig. 1).

All ME observations were made with one-half experiment in an offset configuration to monitor the background. An array swap was effectively performed only in observation 1 (as observation 2 is affected by the above mentioned ADC problem); therefore in most cases it was mandatory to use slew data as

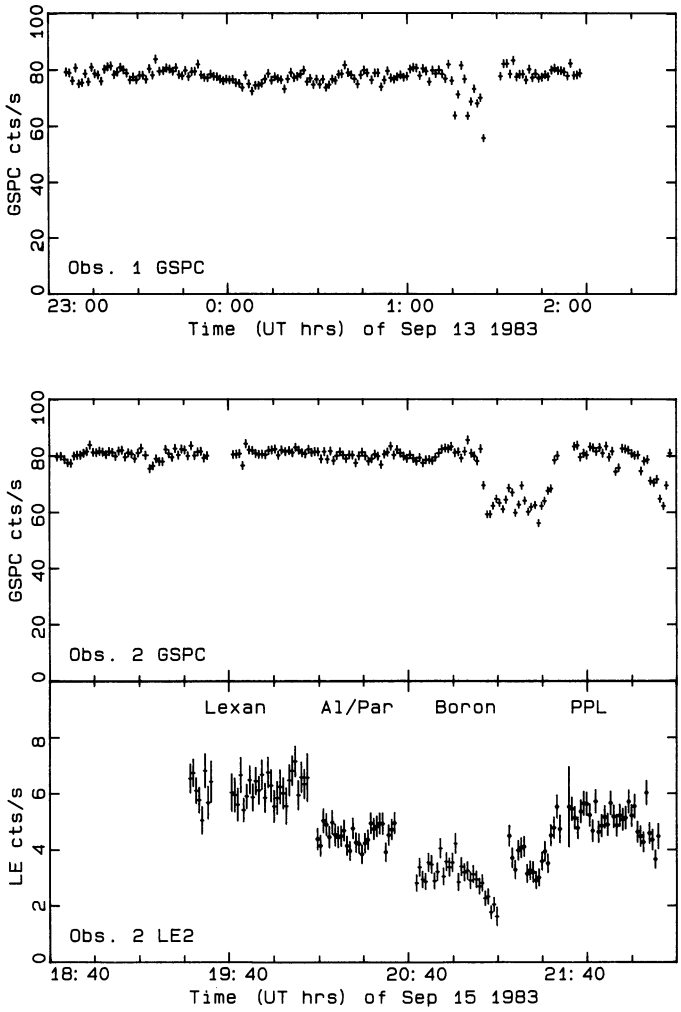

FIG. 1.—GSPC (2–16 keV) and LE2 light curves for observations 1 and 2 containing a dip. Bin sizes are, respectively, 64 s for the GSPC and 60 s for the LE2 light curves. The top panel shows the GSPC light curve for observation 1. No simultaneous data were available in the LE experiments during the dip. The bottom panels show the GSPC and LE2 light curves for observation 2. Note that the LE2 observation is split in four parts, in which different filters were used. The different transmission of the filters is responsible for the different count rate levels. However, the dip is clearly visible at the end of the boron observation and at the beginning of the polypropylene one. Note that the dip ingress observed in the LE + boron filter is slower than that in the GSPC.

background. Additional constraints in the selection of the background data derive from the different operative modes used (compression, absence of Xenon data, etc.).

For all the spectra (accumulated over the entire observing interval) the background observed in the same experiment away from Cyg X-2 was subtracted directly from the source data. On the other hand, for light curves in a given energy range we have instant-by-instant subtracted the simultaneous background in the offset half and then added the compensation factor (the integral in the same energy range of the background difference in the two halves). In the case of observation 1 the spectra from the two ME halves have been combined for fitting (see next section).

We have accumulated ME light curves in a number of different energy ranges. ME light curves in the 1–16 keV range have been published in Chiappetti *et al.* (1987); they show no evidence of significant variability, except for the fact that the flux in observation 3 is at a level of 30% below the other four observations. This is apparent also from the average count rate levels reported in Table 1. The flux decrease is also found in the LE filters. Note that there are no valid ME spectral data in the second half of observation 2 (the one affected by ADC problems), and therefore no reliable light curve can be constructed (see Chiappetti *et al.* 1987).

GSPC light curves and spectra were accumulated in the energy range 2–16 keV. Background subtraction was performed by making use of the slew data to and away from Cyg X-2. The absolute gain was calibrated on the basis of the positions in the pulse height spectra of the contaminating lines at $\sim$11 and 13 keV, which are primarily due to fluorescence of lead in the collimator.

The GSPC light curves for observations 1 and 2 are shown in Figure 1. Note the dip at the end of the first observation and during the second one. Unfortunately, during the dip in observation 1, all other experiments were switched off, while during the dip in observation 2 the ME data were affected by the above-mentioned ADC problem. Only the LE2, with boron and polypropylene filters for part of the time, can be used to obtain some limited spectral information (see Fig. 1 and § IV*d*).

IV. THE 0.1–20keV CONTINUUM; DETECTION OF LINE EMISSION

a) 0.1–20 keV *LE* + *ME Spectrum*

In this section we discuss the average continuum spectrum for each of the five observations. We used ME and LE2 broadband filter data to parameterize the continuum in terms of a simple two-component spectral model, which was then used to analyze the 1000 line mm^{-1} TGS data, to search for discrete emission features in the 0.1–2 keV band. The GSPC data were analyzed similarly, and an emission feature near 6.7 keV was found.

For each observation, we accumulated an average 1–20 keV ME spectrum by combining 1–10 keV data from the argon counters, and 7.5–20 keV data from the xenon counters. The overlap was chosen in order to match the signal-to-noise ratio in the overlapping range. The ME data were supplemented by the simultaneously measured LE2 filter count rates. We fitted each spectrum with a two-component thermal bremsstrahlung plus blackbody model, attenuated by absorption by intervening neutral gas. Best-fitting values for the spectral parameters, and equal-confidence intervals were estimated using the customary χ^2 statistic (see, e.g., Lampton, Margon, and Bowyer, 1976). Free parameters in the model were kT_{tb}, kT_{BB} (the bremsstrahlung and blackbody temperatures), the normalizations of each component, and the column density of neutral gas to the source, N_H. Cross sections for photoelectric absorption by neutral gas (at cosmic abundances) were taken from Morrison and McCammon (1983).

Table 2 lists the best-fitting values of these parameters, for each observation. The quoted luminosities refer to the unabsorbed luminosities at the source, assuming a distance of 8 kpc. The extreme values are for 99% confidence for three parameters of interest (the temperatures, and the column density). Figure 2 shows two examples of fits to ME plus LE2 filter data, for observations 1 and 3, respectively, while Figure 3 gives the contours in the two-temperature plane for all the observations.

We also tried fitting single-component models (bremsstrahlung, blackbody, or power-law), and Comptonization models, but both classes of models were found to give statistically unacceptable fits to the data.

TABLE 2

SPECTRAL FITS

Observation Number (1)	N_H (10^{21} cm^{-2}) (2)	Min/Max (3)	T_{tb} (keV) (4)	Min/Max (5)	T_{bb} (keV) (6)	Min/Max (7)	L_{tb} (10^{38} ergs sec^{-1}) (8)	Min/Max (9)	L_{bb} (10)	Min/Max (11)	L_{ov} (12)	Min/Max (13)	χ^2 (14)	d.o.f. (15)
1.....	2.0	1.8 2.2	4.4	4.3 4.6	1.21	1.17 1.24	1.32	1.27 1.34	0.385	0.380 0.399	1.71	1.67 1.73	2.6	45
2.....	2.2	2.1 2.5	4.2	4.0 4.4	1.21	1.17 1.25	1.36	1.33 1.39	0.369	0.362 0.377	1.73	1.70 1.76	1.8	41
3.....	2.1	2.0 2.3	6.2	5.9 6.7	1.74	1.58 1.87	1.07	1.05 1.08	0.124	0.109 0.137	1.19	1.18 1.20	1.5	45
4.....	2.6	2.4 2.8	6.1	5.9 6.4	1.48	1.43 1.55	1.43	1.41 1.46	0.290	0.282 0.297	1.72	1.71 1.74	3.6	51
5.....	2.4	2.2 2.5	6.5	6.2 6.8	1.49	1.44 1.55	1.27	1.24 1.29	0.303	0.296 0.316	1.57	1.55 1.59	2.4	50

Col. (1)—Observation sequence number used in text.

Cols. (2)–(3).—Best-fit values of the hydrogen column density for a thermal bremsstrahlung (tb) model + blackbody model (BB). (col. [2]) and extremes of the 99% confidence interval (col. [3]).

Cols. (4)–(5).—Best-fit values of the temperature of the bremsstrahlung component [col. (4)] and extremes of the 99% confidence interval (col. [5]).

Cols. (6)–(7).—Best-fit values of the temperature of the blackbody component (col. [6]) and extremes of the 99% confidence interval (col. [7]).

Cols. (8)–(13).—Luminosities at the source for the bremsstrahlung (cols. [8]–[9]), the blackbody (cols. [10]–[11]) components, and overall (cols. [12]–[13]), calculated in the band 0.1–20 keV, for a distance of 8 kpc.

Col. (14).—Reduced χ^2 of the best-fit spectrum.

Col. (15).—Number of degrees of freedom.

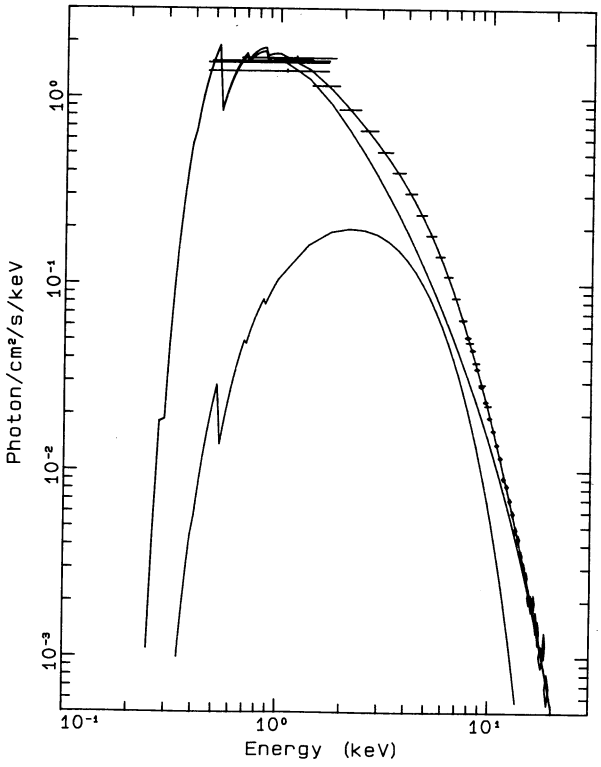

FIG. 2*a*

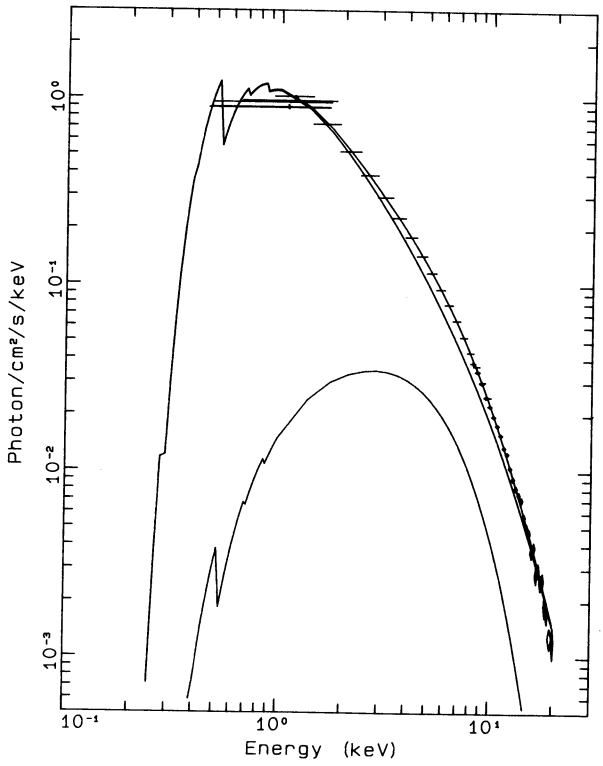

FIG. 2*b*

FIG. 2.—Reconstructed LE + ME photon spectra for high-level observation 1 on 1983 September 13 (*a*) and low-level observation 3 on 1983 September 18 (*b*). LE filter data are indicated with error bars corresponding to the interval including 90% of the flux. ME argon data are also indicated as error bars, while ME xenon data are indicated as diamonds. The overall best fit and the two separate components bremsstrahlung (*upper curve*), and blackbody (*lower curve*) are shown.

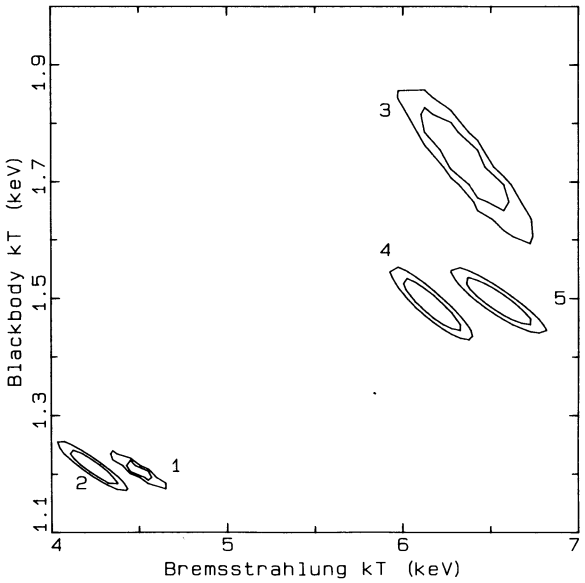

FIG. 3.—The projection of the 90% and 99% confidence contours plotted in the two-temperature plane as derived from the LE + ME fits. The numbers correspond to the observation sequence number. Note that the contours have been calculated considering three interesting parameters (the third being the hydrogen column density).

The total 0.1–20 keV luminosity is roughly constant, at $L_X \sim 1.7 \times 10^{38}$ ergs s^{-1}, except for observation 3 when the source was some 30% fainter. On the basis of the temperature of the two components observation 3 appears close to observation 4 and 5, while 1 and 2 are distinct (see Fig. 3). The temperatures that we find are generally consistent with previous and subsequent measurements. The column density is roughly consistent with the value calculated from the reddening E_{B-V} (Chiappetti *et al.* 1983; McClintock *et al.* 1984), using the mean reddening-column density relation determined by Bohlin, Savage, and Drake (1978).

b) 0.5–2 keV *TGS Spectrum*

The LE transmission grating spectral data were reduced as follows. A rectangular "box" was constructed in the image along the dispersion direction, 20 pixels wide in the cross-dispersion direction. A raw spectrum (counts vs. pixel number) was extracted by integrating all the counts in the direction perpendicular to the dispersion. The median of the zero-order peak was taken as the zero-order position, and the dispersion relation was used to convert pixel numbers to wavelengths. For analysis purposes, the spectrum was binned in 0.5 Å (2 pixel) bins.

A number of background histograms were obtained using boxes 20 pixels wide, centered on the zero-order position, and rotated with respect to the dispersion direction. These histograms were averaged and smoothed. The resulting profile was used as an estimate of the level of nondispersed radiation (background plus contamination by the zero-order image) under the spectrum. The zero order was found to contribute over 50% of the counts shortward of the position corresponding to ~ 5 Å, and as a measure of caution, spectral fluxes shortward of this limit were excluded from the detailed analysis. Spatial variations in detector efficiency are almost entirely negligible over the area on the detector occupied by the first order spectrum (differential variations less than $\sim 2\%$). Finally, constant correction factors were applied to the spectrum to take account of the reduction in efficiency of the optics at the off-axis position of the source, and counts lost below the LE pulse height window cutoff (both corrections less than 5%).

The resulting spectrum was analyzed by folding model spectra through the spectrometer response, adding higher orders and background, integrating in bins corresponding to the measured spectrum, and fitting them to the measured spectrum. The quality of the fits was judged with the customary χ^2-statistic, which also yielded regions of equally acceptable values for the spectral parameters (Lampton, Margon, and Bowyer 1976). We required models to fit both the negative and positive spectral orders separately, as a consistency check on the data reduction procedure.

Preliminary inspection of the spectrum showed that first-order dispersed radiation was significantly detected from Cyg X-2 in the band 5–23 Å; at longer wavelengths, higher spectral orders dominate over the first order. In this region, the spectrometer response profile is determined by the optics and is almost completely independent of wavelength. Consequently the zero-order image, integrated perpendicularly to the dispersion direction, can be used as an accurate and self-consistent representation of the spectrometer response. We constructed such a profile from the zero-order image in our data, extrapolated with empirical power laws in counts versus pixel number, beyond ~ 20 pixels from the center of the profile, to describe the wings of the spectrometer profile.

Next, we used the continuum model determined by the ME and LE2 filter data, to analyze the 100 line mm^{-1} TGS data obtained during observation 1. The first-order grating spectrum covers the band 5-23 Å and is therefore almost completely insensitive to the bremsstrahlung and blackbody temperatures, but it is extremely sensitive to N_H. We therefore chose to fix kT_{tb} and kT_{BB} at the best fitting values for observation 1 and fit the grating data with N_H as free parameter. Initial test fits indicated that the cross-calibration between the ME and the 1000 line mm^{-1} TGS is correct to within a few percent, so that we may confidently extrapolate the ME spectrum directly into the TGS band.

When we fitted the full range of the grating data we found that acceptable fits at parameter values close to those indicated by the ME spectrum were not possible. Inspecting the spectrum we noted a systematic excess of the measured spectrum over the models in the restricted range 12–19 Å. Excluding this range improved the fits significantly, driving χ^2 down to 78 (82 degrees of freedom [d.o.f.]) for the best fit, from 198 (109 d.o.f.). The excess is therefore significant at the 99% or greater level, with respect to the best fit, for the spectral models assumed. Figure 4 shows the resulting best fit to the grating data. Post-fit residuals are shown in the lower panel, plotted as the number of standard deviations by which the counts in each bin exceed the predicted continuum level.

The excess seen with respect to the continuum model in the 12–19 Å range cannot be attributed to instrumental effects. In our band the grating spectrometer efficiency was calibrated at 7.04, 8.25, 13.2, and 23.6 Å. While there is a small ($\leq 15\%$) uncertainty in the interpolation of efficiencies between these wavelengths (see, Paerels *et al.* 1989), the *shape* of the observed excess (a broad "hump" extending from 12–19 Å) is not consistent with possible "humps" that could be due to calibration errors. Moreover, the efficiency at 13.2 Å (a calibration point) would have to be in error by $\sim 20\%$ with respect to the other calibration points in order to explain the excess in the Cyg X-2

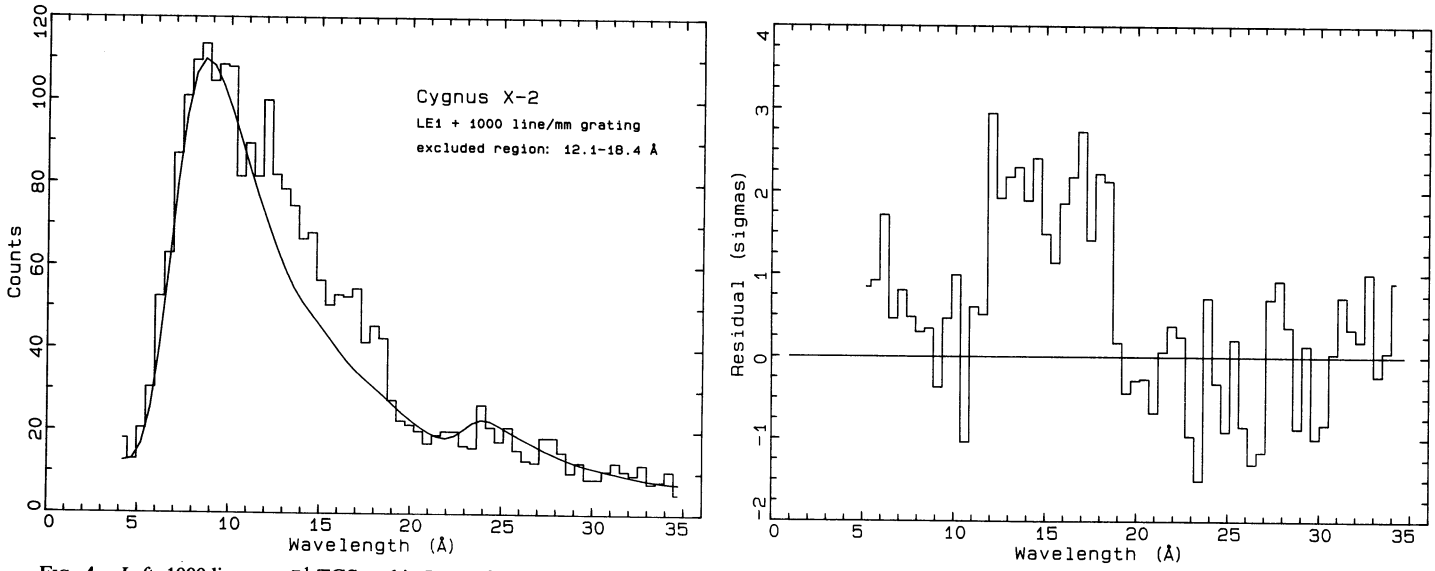

FIG. 4.—*Left*: 1000 lines mm^{-1} TGS + thin Lexan filter spectrum (*histogram*), measured during observation 1, and model spectrum (*solid line*) for Cyg X-2. The model includes contributions from nondispersed radiation (constant detector background, zero-order); negative and positive spectral orders are summed. First-order dispersed photons were detected between 5 and 23 Å. Longward of 23 Å higher orders dominate. The wavelength region 12.1–18.4 Å was excluded from the fit. The model spectrum is based on the best fit to the simultaneous ME data, with the column density optimized to fit the grating spectrum. *Right panel*: Post-fit residuals, divided by the variance predicted from photon-counting statistics, based on the continuum model. A significant excess over the continuum is seen between 12 and 19 Å.

spectrum, which is unlikely. We therefore identify the excess with unresolved emission line complexes. However, we cannot exclude the possibility that part of the excess in the restricted 15–19 Å range is due to small systematic errors in the adopted shape of the grating efficiency curve.

We find the column density of neutral absorbing gas to be in the range $N_H = 1.9–2.2 \times 10^{21}$ cm^{-2} (99% confidence), consistent with the value found from the ME plus LE2 filter data (see Table 2). The grating data in principle allow one to determine column densities of the various absorbers (both neutral and ionized) separately, by direct absorption spectroscopy.

Of the most abundant neutral species, only oxygen has a strong absorption edge in the wavelength range spanned by our first-order spectrum, the K edge at 23 Å. To determine the neutral oxygen column density, we fitted the spectrum with absorption by neutral gas at cosmic abundances, excluding oxygen, at equivalent hydrogen column density N_H, and added the oxygen absorption separately. Both N_H and A_{ox}, the abundance of oxygen relative to cosmic, were allowed to vary in the fit. Figure 5 shows the resulting joint 90 and 99% confidence regions for joint estimate of these two parameters. The oxygen abundance is consistent with cosmic, with 90% confidence limits of 0.5–1.3 times cosmic.

No edges due to ionized species, such as those due to the hydrogen- and helium-like ions of oxygen and nitrogen, were seen in the data. However, the limited statistics of the data do not allow us to set astrophysically meaningful upper limits on the corresponding column densities.

c) 2–15 keV *GSPC Spectrum*

We now turn to the GSPC data. In principle, an analysis as described for the ME data can also be carried out for the GSPC. The distinguishing feature of this instrument is its higher energy resolution, so we used it primarily to look for discrete Fe emission between 6.4 and 7 keV. Also, the GSPC was the only hard X-ray detector operative at the time of the two intensity dips during observations 1 and 2, and so we used it to look for variations in the spectral characteristics across the dips.

We accumulated average 2–15 keV spectra for all five observations; the dip intervals were excluded from observations 1 and 2. A two-component exponential plus blackbody model, similar to that used for the ME analysis, was fitted to the data. The column density was initially held fixed at $N_H = 2 \times 10^{21}$ cm^{-2}, since the GSPC data are insensitive to columns less than 10^{22} cm^{-2}. Iron line emission was included in the model with the centroid energy, and total line photon flux allowed to float in the fitting procedure.

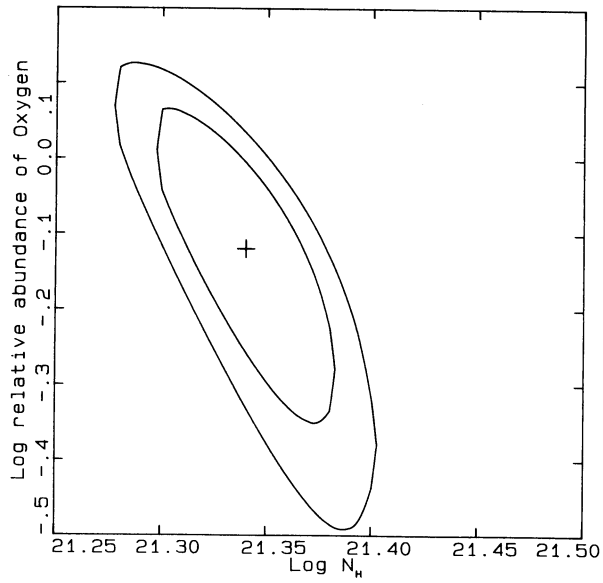

FIG. 5.—90% and 99% confidence contours for joint estimate of the column density of neutral absorbing gas, N_H, and oxygen abundance in the column (relative to cosmic abundance), as measured from the 23 Å oxygen K absorption edge in the grating spectrum.

TABLE 3

OBSERVATIONS OF THE DISCRETE IRON FEATURE WITH THE GSPC

Observation Number	Line Energy (keV)	Equivalent Width (eV)	Notes
1.....	6.67 ± 0.07	60 ± 8	outside of dip
1.....	...	<41	within dip
2.....	6.67 ± 0.10	55 ± 7	outside of dip
2.....	...	<33	within dip
3.....	6.86 ± 0.14	34 ± 12	
4.....	6.69 ± 0.20	14 ± 9	
5.....	6.57 ± 0.23	18 ± 8	

In all cases we obtained best fitting values for the continuum parameters that were consistent with the values derived from the ME data. Iron line emission was detected significantly during observations 1, 2, and 3 (e.g., for observation 1, including the line lowered minimum χ^2 from 305 [203 d.o.f.] to 225 [201 d.o.f.]). The detection was marginal for the other observations, consistent with no line emission required for an acceptable fit. Table 3 lists the line centroid energies and equivalent widths for all observations, together with the 90% confidence intervals for these parameters. Figure 6 shows an example of a GSPC spectrum, together with the best-fitting model with the line strength set to zero; the lower panel displays the post-fit residuals, which show the 6.7 keV emission feature. We note that *Tenma* observed very similar line characteristics, in an observation that took place one week after our observations 1 and 2 (Hirano *et al.* 1987).

d) Spectral Variations across a Dip

Next, we carried out a similar analysis on the GSPC data for the two dip-intervals. Table 4 lists best-fitting continuum spectral parameter values, both outside and during the dips. These were obtained by simultaneously fitting GSPC and LE2 broad-band filter data, allowing for changes in N_H during the dips. We only list results for observation 2; the data accumulated in the dip during observation 1 are of too low statistical quality to allow a meaningful comparison with the nondip data, and also there are no LE data. As can be seen from Table 4, the spectrum hardens across a dip, the column density remains constant within the statistical errors, accompanied by a drop in total unabsorbed flux.

The best-fitting models indicate that no line emission is required during the dips, with 90% confidence upper limits on the equivalent widths of 41 and 33 eV for observations 1 and 2, respectively. Compared with the positive detections of line emission outside the dips (EW of 60 ± 8, and 55 ± 7 eV, respectively), these limits indicate a marginally significant change (~3 σ) in the line emission characteristics across the dips.

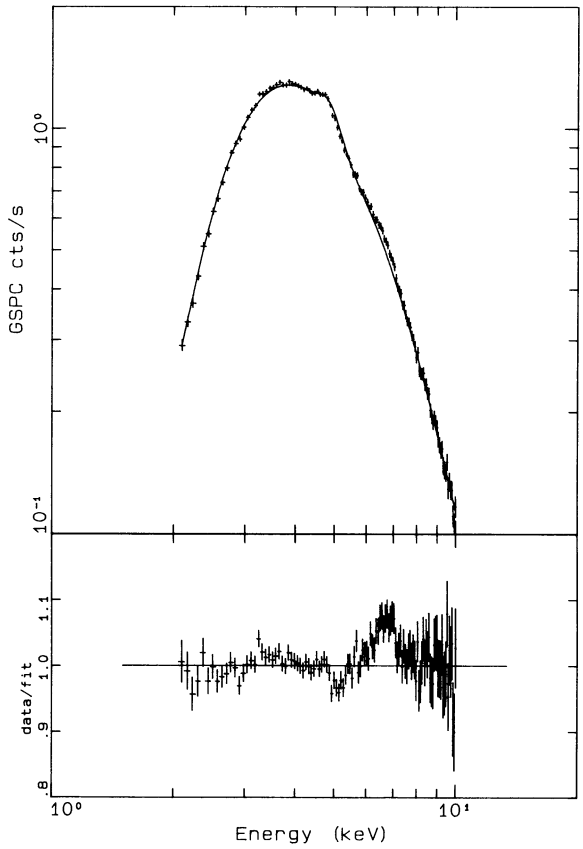

FIG. 6.—The top panel shows the GSPC counts spectrum for observation 1. The solid line is the thermal plus blackbody best-fit continuum, with the parameters obtained including an Fe line in the fit, but with the Fe line intensity set to zero. The bottom panel is a rectified spectrum, i.e., the data divided by the above plotted best fit. A line feature at ~4.7 keV is inherent to the GSPC and is due to a gain discontinuity in the detector. Its presence is taken into account in the spectral fitting procedure.

V. *IUE* SPECTRA

A journal of the IUE observations is reported in Table 5. The spectra SWP 21087 and SWP 21134 partially overlap with *EXOSAT* observations 3 and 5, respectively, while SWP 21112 is displaced by a few hours with respect to observations 4. All three spectra are underexposed and rather noisy. The spectra were extracted by using a local implementation within the ESO-IHAP software of the Gaussian Extraction Procedure originally developed by Urry and Reichert (1988). It was found that the only wavelength intervals where the continuum flux can be reliably measured is 1800–1860 Å (see Table 5). The

TABLE 4

GSPC CONTINUUM FIT PARAMETERS ACROSS DIP (OBSERVATION 2)

Observation Interval (within/outside dip)	N_H (cm^{-2})	kT_{bb} (keV)	kT_{BB} (keV)	L_{bb}[a] (10^{38} ergs s^{-1})	L_{BB}[a]	χ^2 (per d.o.f.)
Dip: GSPC(2.7–16 keV)+PPL+B[b].....	2.3 ± 0.30	5.1 ± 0.30	1.23 ± 0.05	0.30	0.20	1.0
No dip: GSPC(2.7–16 keV)+PPL+B.....	2.5 ± 0.20	4.3 ± 0.10	1.09 ± 0.02	0.39	0.23	1.2

[a] Luminosities at the source are in the range 2.7–16 keV.

[b] PPL, B: the polypropylene and boron filters on LE2. Error limits are 90% confidence.

TABLE 5

SUMMARY OF *IUE* OBSERVATIONS

Camera and Image Number	Start Time Date (1983)	Start Time UT	Exposure Time (minutes)	Flux (1800–1860 Å) (10^{-15} ergs cm^{-2} s^{-1} Å^{-1})	*EXOSAT* Observation Number	*EXOSAT* Observation UT
SWP 21087.....	Sep 18	14:37	188	4.1 ± 0.1	3	16:05
SWP 21112.....	Sep 20	18:25	172	2.3 ± 0.1	4	23:22
SWP 21134.....	Sep 22	14:49	176	2.4 ± 0.1	5	15:51

internal error is ~5%, and the *IUE* photometric accuracy is 10%. The state of September 18 is clearly brighter than those of September 20 and 22, while in the X-rays September 18 corresponds to the weaker state.

Comparing with our previous *IUE* observations of 1979–1980 (see Chiappetti *et al.* 1983), we find that SWP 21112 and SWP 21134 corresponds to the weakest detected UV states. Several emission lines are present. Because of the flaws and the noise we were able to measure only N v λ1240 in SWP 21987, obtaining an equivalent width of 20 Å, which is the lowest value detected for this line (Chiappetti *et al.* 1983).

VI. DISCUSSION

a) Position in the HR/Intensity Plane

To obtain a rough empirical description of the intensity and spectral behavior of the source we constructed the, by now conventional, hardness-intensity and X-ray color-color diagrams. For each of our observations we accumulated total hard X-ray intensity and spectral hardness (defined as the total ME 1–17 keV count rate per half experiment, and the ratio of count rate in the 6–17 to the rate in the 3–6 keV band, respectively) in 60 s intervals. Figure 7*a* shows the resulting hardness-intensity diagram; the clusters of points corresponding to the different observations are labeled by the sequence number. Using the same time intervals we also constructed a color-color diagram (Fig. 7*b*), plotting the "hard hardness" as defined above, against the "soft hardness," defined as the ratio of count rates in the 3–6 and 1–3 keV bands.

Figures 7*a*–7*b* clearly show the bimodal behavior first seen in *Copernicus* data by Branduardi *et al.* (1980), in *Einstein* data by Vrtilek *et al.* (1986), and *EXOSAT* data by Hasinger *et al.* (1986). It has been shown that part of the time Cyg X-2 moves along an apparently unique, Z-shaped track in the X-ray color-color diagram (Hasinger, Priedhorsky, and Middleditch 1989; Hasinger *et al.* 1989), a property that seems to be universal among the majority of LMXB's (Schulz, Hasinger, and Trümper 1989).

Observations 1 and 2 fall on the lower "normal branch" of the Z (intensity positively correlated with spectral hardness), observations 3 is on the "horizontal branch" (no correlation between intensity and hardness), while observations 4 and 5 are in the region where these two branches meet (note that the pattern shown in our diagram is slightly offset from the corre-

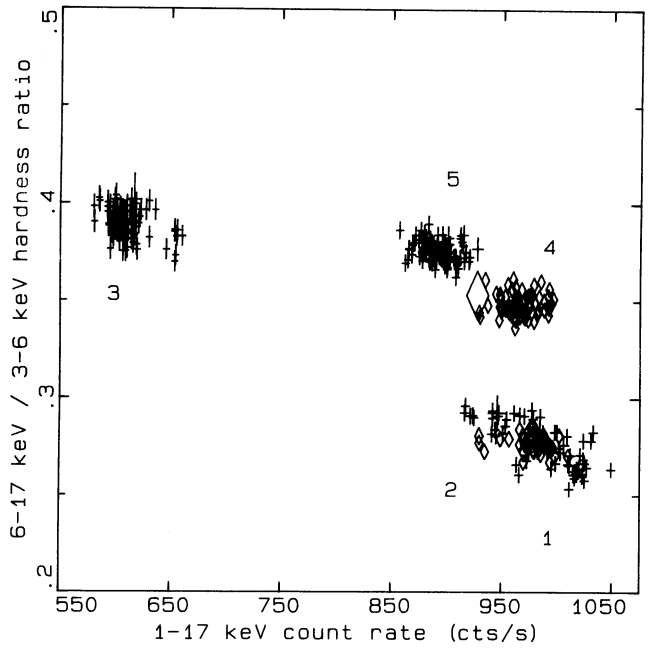

FIG. 7a

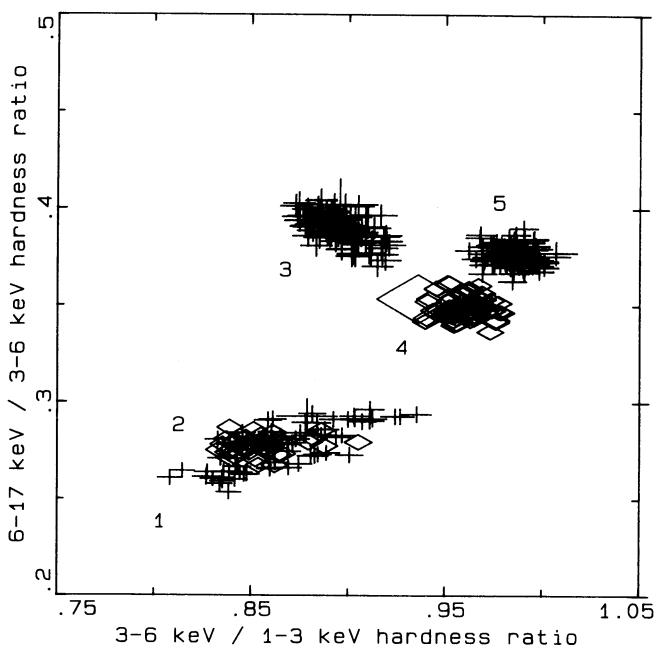

FIG. 7b

FIG. 7.—The 6–17 keV to 3–6 keV hardness ratio is plotted vs. the total count rate (in counts s^{-1} per half) in panel (*a*), and vs. the 3–6 to 1–3 keV hardness ratio in panel (*b*). Individual points have a nominal resolution of 60 s. The numbers correspond to the observation sequence numbers. For clarity, odd-numbered observations (1, 3, 5) are shown as error bars, and even-numbered observations (2, 4) as diamonds. The two plots can be compared with Fig. 1 of Schulz *et al.* (1989), which reports a larger set of data, and clearly indicates the Z shape of the color/color diagram.

sponding pattern in the diagrams presented by Schulz, Hasinger, and Trümper (1989), because of a slightly different choice of pulse height channels used to define the three energy bands).

b) *Modulation with Orbital Phase*

A substantial progress in understanding the nature of the Cyg X-2 was consequent the discovery of the 9.8 day binary period (CCH). The detection of the same periodicity in the X-ray data is a controversial issue. Some evidence in this sense is reported by Vrtilek *et al.* (1986), who found a significant correlation of *Einstein* Monitor Proportional Counter counts with the *U* light curve of CCH.

On the basis of the same data and of data from other satellites Vrtilek *et al.* (1986) found that the occurrence of dips is concentrated near phase 0 (inferior conjunction of the X-ray source). The same behavior is also found by Bonnet-Bidaud and van der Klis (1982) in the *COS B* data. It is notable that in our data the large dips appear in observation 1 ($\phi = 0.8$) and 2 ($\phi = 0.0$), while they are absent in 3, 4, and 5 ($\phi = 0.3$, 0.5, and 0.7). The occurrence of dips in this phase range would be consistent with "bulges" on the outer rim of the accretion disk intercepting our line of sight to the central X-ray source, possibly associated with the impact of the accretion stream from the secondary on the disk.

Besides the presence of dips and the hardness of the spectrum, observations 1 and 2 are different because of the higher intensity of the Fe line (see § IV*c*). Again, it is difficult to claim that a phase dependence is established, but it may be significant that CCH indicate that the emission of He II λ4686 is strongest at phase 0, when the line of sight intercepts a stream of matter from the non collapsed component to the neutron star (see Fig. 5 of CCH).

An interpretation of the X-ray intensity variation as phase dependent is even less convincing. In fact, the only significant variation observed in our data is that in observation 3 ($\phi = 0.33$), when the source is clearly in a lower state than during observations 1, 2, 4, and 5, while the light curves from the *Einstein Observatory* data indicate a clustering of high states between $\phi = 0.25$ and $\phi = 0.45$.

c) *Spectral Changes During Dips*

We briefly discuss possible explanations for the spectral changes observed during the two intensity dips. As described above, the continuum spectrum hardens significantly across a dip, at constant apparent column density of absorbing neutral gas, while the total unabsorbed 0.5–20 keV flux appears to drop.

Curiously, this is almost the exact opposite of what was seen in the *Einstein* OGS + Monitor Proportional Counter data by Vrtilek *et al.* (1986). In terms of a simple bremsstrahlung model, they found that $kT_{\rm ib}$ remained constant across a dip, while $N_{\rm H}$ increased significantly, accompanied by a significant drop in total unabsorbed flux. This particular behavior naturally suggests an explanation of the dips as absorption events of some sort, in which an extended hard X-ray source (e.g., an accretion disk corona) is obscured by clumps of matter crossing the line of sight.

Our data appear to be in conflict with this simple, intuitive picture. However, it must be remembered that the spectral parameterization in terms of a superposition of thermal bremsstrahlung and a blackbody is merely one of convenience. Given the limited energy resolution of proportional counters, it is perhaps conceivable that both the apparent increase in spectral temperature and overall decline of flux at constant $N_{\rm H}$ (seen in our data), or increased absorption and decline in flux at constant spectral temperature (seen in the *Einstein* data) across a dip are to some extent artifacts of the parameterization. The spectral variations could perhaps also be due to selective absorption of a spectrally unresolved, soft component arising in an emission region of geometric dimensions smaller than the region that emits the bulk of the harder photons (e.g., an accretion disk corona). This would account for the apparent hardening of the spectrum and decline in flux seen both by *Einstein* and *EXOSAT*. Because of the limited resolution of the available data this issue must for now remain unresolved.

d) *Origin of the X-Ray Lines*

Finally, we briefly discuss possible explanations of the 6.7 keV emission and the soft X-ray emission lines. The emission feature at 6.7 keV may be attributed to helium-like Fe K shell emission broadened by multiple Compton-scattering. The equivalent widths we determined are similar to those detected in other LMXBs. The feature is present in the two observations in which the source is on the lower normal branch of the "Z" in the X-ray color-color diagram, a finding consistent with recent results from *Ginga* (Hasinger *et al.* 1989). We note, however, that the exact equivalent width, and the preference for detection on the lower normal branch are properties that appear to be rather sensitive to the exact continuum parameterization adopted (Hasinger *et al.* 1989).

We find evidence for a marginally significant drop in the equivalent width of the iron line across the dips observed during observations 1 and 2. This may indicate that the line emission arises in a region more compact than the continuum-emitting region (presumably an accretion disk corona).

The appearance of discrete excess emission in the soft X-ray grating spectrum, in the range 12–19 Å, confirms the detection of similar features for Cyg X-2 and other sources in the *Einstein* OGS data. The features are most likely associated with a complex of Fe L-shell emission lines produced in a moderate density plasma ($n_e \sim 10^{11}$ cm^{-3}) located near the edge of the accretion flow. Such material will be photoionized by the strong X-ray continuum emission from the central source, and the lines are mostly excited by radiative cascades following recombination. The features observed with *EXOSAT* are similar to, but not identical with, the ones detected with *Einstein*. This is to be expected, since moderate changes in the ionizing flux, or the density and geometry of the accreting flow can produce qualitative changes in the details of the discrete emission spectrum. At present, the limited spectral resolution of the data precludes a sophisticated analysis, included a precise identification of the lines.

P. E. F., F. B. S. P., and S. M. K. acknowledge the support of grants from the NASA Astrophysics Data Program, the NASA Innovative Research Fund, and the University of California Campus–Laboratory Collaborative Research Fund.

REFERENCES

Bohlin, R. C., Savage, B. D., and Drake, J. F. 1978, *Ap. J.*, **224**, 132.
Bonnet-Bidaud, J. M., and van der Klis, M. 1982, *Astr. Ap.*, **116**, 232.
Bradt, H. V., and McClintock, J. E. 1983, *Ann. Rev. Astr. Ap.*, **21**, p. 13.
Branduardi, G., Kylafis, N. D., Lamb, D. Q., and Mason, K. O. 1980, *Ap. J. (Letters)*, **235**, L153.
Chiappetti, L., Ciapi, A., Maraschi, L., Stella, L., Tanzi, E. G., and Treves, A. 1987, *Ap. Space Sci.*, **131**, 691.
Chiappetti, L., Maraschi, L., Tanzi, E. G., and Treves, A. 1983, *Ap. J.*, **265**, 354.
Cowley, A. P., Crampton, D., and Hutchings, J. B. 1979, *Ap. J.*, **231**, 539 (CCH).
Crampton, D., and Cowley, A. P. 1980, *Pub. A.S.P.*, **92**, 147.
de Korte, P. A. J., *et al.* 1981, *Space Sci. Rev.*, **30**, 495.
Freeman, P. E., *et al.* 1989, *IAU Colloquium 115, High-Resolution X-Ray Spectroscopy of Cosmic Plasma*, eds. P. Gorenstein and E. Zombeck (Cambridge: Cambridge University Press), in press.
Hasinger, G., Langmeier, A., Sztajno, M., Trümper, J., Lewin, W. H. G., and White, N. E. 1986, *Nature*, **319**, 469.
Hasinger, G., Priedhorsky, W. C., and Middleditch, J. 1989, *Ap. J.*, **337**, 843.
Hasinger, G., van der Klis, M., Ebisawa, K., Dotani, T., and Mitsuda, K. 1989, *Astr. Ap.*, in press.
Hirano, T., Hayakawa, S., Nagase, F., Masai, K., and Mitsuda, K. 1987, *Pub. Astr. Soc. Japan*, **39**, 619.
Lampton, M., Margon, B., and Bowyer, C. S. 1976, *Ap. J.*, **208**, 177.
McClintock, J. E., Petro, L. D., Hammerschlag-Hensberge, G., Proffitt, C. R., and Remillard, R. A. 1984, *Ap. J.*, **283**, 794.
Mitsuda, K., *et al.* 1984, *Pub. Astr. Soc. Japan*, **36**, 741.
Morrison, D., and McCammon, D. 1983, *Ap. J.*, **270**, 119.
Paerels, F. B. S., Brinkman, A. C., den Boggende, A. J. F., de Korte, P. A. J., and Dijkstra, J. 1989, *Astr. Ap.*, submitted.
Peacock, A., *et al.* 1981, *Space Sci. Rev.*, **30**, 525.
Schulz, N. S., Hasinger, G., and Trümper, J. 1989, *Astr. Ap.*, **225**, 48.
Stella, L., Chiappetti, L., Ciapi, A., Maraschi, L., Tanzi, E. G., and Treves, A. 1986, *Proc. 4th Marcel Grossman Meeting on General Relativity*, ed. R. Ruffini (Amsterdam: Elsevier), p. 861.
Turner, M. J. L. T., Smith, A., and Zimmerman, H. U. 1981, *Space Sci. Rev.*, **30**, 513.
Urry, M., and Reichert, A. 1988, *IUE NASA Newsletter*, No. 34.
van der Klis, M. 1989, *Ann. Rev. Astr. Ap.*, **27**, 517.
Vrtilek, S. D., Kahn, S. M., Grindlay, J. E., Helfand, D. J., and Seward, F. D. 1986, *Ap. J.*, **307**, 698.
Webbink, R. F., Rappaport, S. A., and Savonije, G. J. 1983, *Ap. J.*, **270**, 678.
White, N. E., and Peacock, A. 1988, *Mem. Soc. Astr. Italiana*, **59**, 1.
White, N. E., Stella, L., and Parmar, A. N. 1988, *Ap. J.*, **324**, 363.

G. BRANDUARDI-RAYMONT: Mullard Space Science Laboratory, Holmbury St. Mary, Dorking, Surrey RH5 6NT, England, UK

L. CHIAPPETTI and E. G. TANZI: Istituto di Fisica Cosmica del C.N.R., Via Bassini 15a, 20133 Milano, Italy

A. CIAPI, L. MARASCHI, and A. TREVES: Dipartimento di Fisica dell'Universitá, Via Celoria 16, 20133 Milano, Italy

E. N. ERCAN: Physics Department, Boğaziçi University, Bebek, Istanbul, Turkey

P. E. FREEMAN, S. M. KAHN, and F. B. S. PAERELS: Department of Physics, University of California at Berkeley, Berkeley, CA 94720